bradscholars

Analytical and experimental investigations of dam-break flows in triangular channels with wet-bed conditions

Item Type	Article
Authors	Wang, B.;Liu, X.;Zhang, J.;Guo, Yakun;Chen, Y.;Peng, Y.;Liu, W.;Yang, S.;Zhang, F.
Citation	Wang B, Liu X, Zhang J et al (2020) Analytical and experimental investigations of dam-break flows in triangular channels with wet-bed conditions. ASCE Journal of Hydraulic Engineering. 146(10)
DOI	https://doi.org/10.1061/(ASCE)HY.1943-7900.0001808
Rights	(c) 2020 ASCE. Full-text reproduced in accordance with the publisher's self-archiving policy. This material may be downloaded for personal use only. Any other use requires prior permission of the American Society of Civil Engineers. This material may be found at https://doi.org/10.1061/(ASCE)HY.1943-7900.0001808.
Download date	2026-01-12 17:51:06
Link to Item	http://hdl.handle.net/10454/17840

Analytical and experimental investigations of dam-break flows in triangular channels with wet-bed conditions

Bo Wang[1], Xin Liu[2], Jianmin Zhang[3], Yakun Guo[4], Yunliang Chen[5], Yong Peng[6], Wenjun Liu[7], Sha Yang[8] and Fengjie Zhang[9]

[1]Professor, State Key Laboratory of Hydraulics and Mountain River Engineering, Sichuan University, Chengdu, 610065, China. E-mail: wangbo@scu.edu.cn

[2]Master's Candidate, State Key Laboratory of Hydraulics and Mountain River Engineering, Sichuan University, Chengdu, 610065, China. E-mail: 2078995580@qq.com

[3]Professor, State Key Laboratory of Hydraulics and Mountain River Engineering, Sichuan University, Chengdu, 610065, China. ORCID: https://orcid.org/0000-0002-9154-231X. E-mail: zhangjianmin@scu.edu.cn

[4]Professor, Faculty of Engineering & Informatics, University of Bradford, BD7 1DP, UK. E-mail: y.guo16@bradford.ac.uk

[5]Professor, State Key Laboratory of Hydraulics and Mountain River Engineering, Sichuan University, Chengdu, 610065, China. E-mail: 13541291332@163.com

[6]Associate Professor, State Key Laboratory of Hydraulics and Mountain River Engineering, Sichuan University, Chengdu, 610065, P. R. China. E-mail: pengyongscu@foxmail.com (Corresponding author)

[7]PhD student, State Key Laboratory of Hydraulics and Mountain River Engineering, Sichuan University, Chengdu, 610065, China. E-mail: liuwenjun_scu@163.com

[8]Master's Candidate, State Key Laboratory of Hydraulics and Mountain River Engineering, Sichuan University, Chengdu, 610065, China. E-mail:ysha0919@163.com

[9]Master's Candidate, State Key Laboratory of Hydraulics and Mountain River Engineering, Sichuan University, Chengdu, 610065, China. E-mail: 1114139373@qq.com

Abstract: Based on the method of characteristics, an analytical solution for the

one-dimensional shallow-water equations is developed to simulate the instantaneous dam-break flows propagating down a triangular wet bed channel in this study. The internal relationships between the hydraulic properties associated with the dam-break flow are investigated through the comparisons with the well-known analytical solutions for rectangular channels. Meanwhile, laboratory experiments are conducted in a prismatic, horizontal and smooth flume with a triangular cross-section. The non-intrusive digital image processing is applied for obtaining water surface profiles and stage hydrographs. Results show that the dam-break flow propagation depends on the dimensionless parameter h_d^* defined as the ratio of initial tailwater depth over reservoir head. h_d^* has significant effect on the dam-break wave in the downstream flooded area. For $h_d^* \leq 0.4$, the water surface profiles in the reservoir for different h_d^* at a given time remains similar. For $h_d^* \geq 0.5$, extra negative waves occur in the reservoir, leading to the water surface undulations. Undular bores are generated at the dam site and propagate downstream. Time evolution of dam-break flows under three different reservoir heads is similar for the same h_d^*. The inception of water surface profile change is earlier when the reservoir head is larger. The analytical model shows satisfactory agreement with the experimental results though some errors exist between the analytical solution and measurements due to the formation of extra negative waves, jet and undular bores. The similarities and discrepancies between the hydraulics in the triangular and rectangular channels are identified analytically in terms of the profiles of water depth, velocity, discharge, bore height and wave-front celerity with h_d^*. The presented solution could be applied to predict the effect of wet bed condition on the dam-break wave in triangular channels, while laboratory measurement data could be used for validating analytical and numerical models.

Keywords: Dam-break wave; Triangular channel; Wet bed; Analytical solution; Digital image processing.

Introduction

The losses of both properties and human lives caused by dam-break flood wave are considerable, which continuously drives the study of dam-break wave in order to better understand its propagation characteristics for issuing timely flood warning. The investigation on dam-break waves is extremely vital in providing the information for flood risk assessment and for both hazard classification and emergency planning, particularly when the dam is located upstream of heavily populated and industrialized areas. The propagation of dam-break flood waves strongly depends on the cross-sectional shape of river (Su and Barnes 1970; Sakkas and Strelkoff 1973, 1976; Katopodes and Strelkoff 1978; Katopodes and Schamber 1983; Schamber and Katopodes 1984; Wu et al. 1993, 1999; Zanuttigh and Lamberti 2011; Wang et al. 2017). For the sake of convenience, the wide and shallow cross section of rivers is often conceptualized as a rectangle; while the narrow and deep cross section usually is simplified as a triangle.

Due to its practical importance and theoretical interests, extensive studies have been conducted to investigate the dam-break flows in rectangular channels using both the theoretical analysis and laboratory experiments. Ritter (1892) could be considered as the pioneer in dam-break flow study who derived an analytical solution for the hydrodynamic problem of instantaneous dam-break flow in a frictionless and horizontal rectangular channel. Since then, many well-known analytical studies of the dam break have been conducted (Dressler 1952; Whitham 1955; Stoker 1957; Hunt 1982, 1983, 1984; Mangeney et al. 2000; Fernandez-Feria 2006; Hogg 2006; Ancey et al. 2008; Chanson

2009; and Wang et al. 2020a). In addition to analytical study, laboratory experiment is also a popular method for investigating the dam-break flows propagating along the rectangular channel (Dressler 1954; Miller and Chaudhry 1989; Bellos et al. 1992; Fraccarollo and Toro 1995; Lauber and Hager 1998a, b; Stansby et al. 1998; Bukreev and Gusev 2005; Soares-Frazão and Zech 2007; Ozmen-Cagatay and Kocaman 2010; Ozmen-Cagatay and Kocaman 2012; Oertel and Bung 2012; Chen et al. 2013; LaRocque et al. 2013; Ozmen-Cagatay et al. 2014; Kocaman and Ozmen-Cagatay 2015; Liu et al. 2018; Liu et al. 2019; Wang et al. 2019; and Wang et al. 2020b).

Comparing with the extensive studies of dam break flow propagating along rectangular channel, few studies are carried out to investigate the dam-break waves in triangular channels with a wet bed. Sakkas and Strelkoff (1973) analyzed the hydraulics of dam-break floods in a triangular channel with a dry bed. Zanuttigh and Lamberti (2011) highlighted the effect of cross-sectional shape on dam-break wave propagation along channels and presented the celerity, velocity, and bore speed for triangular channels as functions of the relative flow depth difference. An analytical solution for the water surface profiles of dam-break flows in a triangular channel can be obtained through the simplification of the theoretical approach proposed by Wu et al. (1999) for the channel of a trapezoidal cross section. Using the method of Blasius similarity, Chen et al. (2011) obtained analytical solutions which were the same as those of Wu et al. (1999). These analytical solutions are verified by laboratory measurements in a triangular channel with a dry bed conducted by Chen et al. (2011). On the one hand, although the aforementioned analytical models (i.e., Sakkas and Strelkoff 1973; Wu et al. 1999; Zanuttigh and Lamberti 2011; Chen et al. 2011) for dam-break flows in triangular channels were developed by researchers using different approaches, the internal relationships among the hydraulic parameters associated with this phenomenon have not been

appropriately discussed. Moreover, the applicability of analytical solutions remains unknown due to the lack of laboratory data for verification. On the other hand, the effect of wet-bed conditions on the dam-break wave propagation along a triangular channel is poorly understood. Laboratory experiment on the dam-break flow on wet bed with a triangular cross section is required to provide flow features as well as validate analytical solutions. To the authors' best knowledge, few experimental studies have been carried out to investigate the dam-break flows in a triangular channel with a wet bed.

The main objectives of the present study are: (1) to develop analytical solutions of the one-dimensional shallow-water equations for dam-break flows in a triangular channel using the method of characteristics; (2) to collect data on the spatial-temporal evolution of water surface at upstream and downstream of the dam using digital image processing; (3) to evaluate the effect of wet bed condition on the dam-break wave propagation along the channel using both the analytical and physical models; and (4) to validate analytical solutions with the accompanying experiments.

Analytical Model

For an infinitely long horizontal channel of a uniform cross-section, the rarefaction wave and shock wave (or bore) generated by an instantaneous dam break over wet bed is shown in Fig. 1. The structure of the dam-break flow, which is used widely in the development of analytical solutions (Stoker 1957; Wu et al. 1999; Zanuttigh and Lamberti 2011; Wang et al. 2020a), can be divided into four zones down a channel. Zone 1 is the undisturbed water far upstream with reservoir head being equal to h_u and velocity $u_u = 0$. In Zone 2, the rarefaction wave propagates upstream connecting Zone 1 with Section *M-M* (i.e., rarefaction wave front, or called negative wave front) and downstream connecting Zone 3 with Section *N-N* (i.e., rarefaction wave tail). Zone 3 has a constant velocity and

depth (i.e., u_c and h_c) that connects the shock wave (Section *R-R*). Zone 4 is the downstream region with a tailwater depth of h_d and velocity $u_d = 0$, limited upstream by the shock wave that travels with a constant speed ξ.

One-dimensional Equations for Arbitrary Channel Section

The propagation of a dam-break flood resulting from a sudden release of a mass fluid in a channel is governed by the equations of gradually varied unsteady flow in an open channel, the one-dimensional (1D) shallow-water equations (Chow 1959). For an infinitely long prismatic and horizontal channel, if the effect of friction is neglected, the equations can be written as:

$$\frac{\partial h}{\partial t} + u\frac{\partial h}{\partial x} + \frac{A}{B}\frac{\partial u}{\partial x} = 0 \tag{1}$$

$$\frac{\partial u}{\partial t} + u\frac{\partial u}{\partial x} + g\frac{\partial h}{\partial x} = 0 \tag{2}$$

where h = flow depth, x = distance, t = time, g = gravity acceleration, u = mean flow velocity, B = water surface width, A = cross-sectional area.

The initial conditions of the dam-break problem considered in this study can be described by

$$u\big|_{t=0} = 0, \quad h\big|_{t=0} = \begin{cases} h_u & x < 0 \\ h_d & x > 0 \end{cases} \tag{3}$$

where subscripts "u" and "d" = undisturbed far upstream reach and quiet zone downstream, respectively.

The method of characteristics is usually used to solve the system of partial differential equations composed of Eqs. (1–2) which yields a characteristic system of equations:

$$\frac{\mathrm{d}}{\mathrm{d}t}\left(u + \int_0^h \sqrt{g\frac{B}{A}}\mathrm{d}\eta\right) = 0 \qquad \text{along} \quad \frac{\mathrm{d}x}{\mathrm{d}t} = u + \sqrt{g\frac{A}{B}} \tag{4}$$

$$\frac{\mathrm{d}}{\mathrm{d}t}\left(u-\int_0^h\sqrt{g\frac{B}{A}}\mathrm{d}\eta\right)=0 \quad \text{along} \quad \frac{\mathrm{d}x}{\mathrm{d}t}=u-\sqrt{g\frac{A}{B}} \tag{5}$$

where $\int_0^h\sqrt{g\frac{B}{A}}\mathrm{d}\eta$ = Escoffier stage variable (Escoffier 1962; Henderson 1966; Schamber and Katopodes 1984; Wu et al. 1999; Aureli et al. 2014).

Along the forward characteristics, there is

$$\left(u+\int_0^h\sqrt{g\frac{B}{A}}\mathrm{d}\eta\right)-\left(u_u+\int_0^{h_u}\sqrt{g\frac{B}{A}}\mathrm{d}\eta\right)=0 \tag{6}$$

Applying the condition $u_u = 0$ in Eq. (6) yields

$$u=\int_0^{h_u}\sqrt{g\frac{B}{A}}\mathrm{d}\eta-\int_0^h\sqrt{g\frac{B}{A}}\mathrm{d}\eta \tag{7}$$

Since each of the backward characteristics is a straight line, dx/dt can be replaced by x/t for an infinitely long prismatic channel. Eq. (5) can be transformed as

$$\frac{x}{t}=u-\sqrt{g\frac{A}{B}} \tag{8}$$

Substituting Eq. (7) into Eq. (8) yields

$$\int_0^h\sqrt{\frac{B}{A}}\mathrm{d}\eta+\sqrt{\frac{A}{B}}=\int_0^{h_u}\sqrt{\frac{B}{A}}\mathrm{d}\eta-\frac{x}{t\sqrt{g}} \tag{9}$$

The motion of the shock wave is described by the Rankine-Hugoniot equations for mass and momentum:

$$\xi=\frac{A_c u_c-A_d u_d}{A_c-A_d} \tag{10}$$

$$u_c=u_d+\left[g\frac{\left(A_c\bar{h}_c-A_d\bar{h}_d\right)\left(A_c-A_d\right)}{A_c A_d}\right]^{1/2} \tag{11}$$

where subscript "c" = back reach of the shock; $\bar{h}$ = centroid depth for the cross section; ξ = propagation velocity of the shock, so-called shock wave-front celerity, and defined by

$$\xi = \frac{\mathrm{d}x_R}{\mathrm{d}t} \tag{12}$$

in which x_R = shock location shown in Fig. 1, as a function of time t.

Eq. (10–11) can be simplified by applying the condition $u_d = 0$ as:

$$\xi = \frac{A_c u_c}{A_c - A_d} \tag{13}$$

$$u_c = \left[g \frac{\left(A_c \bar{h}_c - A_d \bar{h}_d\right)\left(A_c - A_d\right)}{A_c A_d} \right]^{1/2} \tag{14}$$

The hydraulic characteristics, i.e., flow depth and velocity, are unique in the cross section *N–N* connecting the Zones 2 and 3. Applying Eq. (4) in this boundary condition yields the flow velocity in the Zone 3:

$$u_c = \int_0^{h_u} \sqrt{g \frac{B}{A}} \mathrm{d}\eta - \int_0^{h_c} \sqrt{g \frac{B}{A}} \mathrm{d}\eta \tag{15}$$

Substituting Eq. (14) into Eq. (15) yields the flow velocity:

$$\int_0^{h_u} \sqrt{\frac{B}{A}} \mathrm{d}\eta - \int_0^{h_c} \sqrt{\frac{B}{A}} \mathrm{d}\eta = \left[\frac{\left(A_c \bar{h}_c - A_d \bar{h}_d\right)\left(A_c - A_d\right)}{A_c A_d} \right]^{1/2} \tag{16}$$

Eqs. (9) and (16) are applicable for a prismatic channel with arbitrary cross-sections.

Analytical Solutions for Triangular Channels

For a triangular channel, the cross-sectional area is half of the product of the flow depth and the water surface width. Applying this condition for the rarefaction wave, Eq. (9) can be simplified as:

$$\int_0^{h} \sqrt{\frac{2}{h}} \mathrm{d}\eta + \sqrt{\frac{h}{2}} = \int_0^{h_u} \sqrt{\frac{2}{h}} \mathrm{d}\eta - \frac{x}{t\sqrt{g}} \tag{17}$$

Integrating Eq. (17) yields the dimensionless flow depth

$$h^* = \frac{h}{h_u} = \frac{4}{25}\left(2 - \frac{x}{t\sqrt{2gh_u}}\right)^2 \tag{18}$$

Let

$$\frac{x}{t\sqrt{gh_u}} = \frac{X}{T} \tag{19}$$

where X = dimensionless distance from the dam site, $X = x/h_u$; and T = dimensionless time, $T = t(g/h_u)^{1/2}$. A simplified form of Eq. (18) can be obtained as:

$$h^* = \frac{2}{25}\left(2\sqrt{2} - \frac{X}{T}\right)^2 \tag{20}$$

Let $h^* = 1$, the dimensionless location and celerity of the negative wave front are obtained as:

$$X_M = C_1^* T \tag{21}$$

$$C_1^* = -\frac{\sqrt{2}}{2} \tag{22}$$

Applying Eq. (20) in Eq. (8) yields the dimensionless velocity:

$$u^* = \frac{u}{\sqrt{gh_u}} = \frac{2}{5}\left(\sqrt{2} + 2\frac{X}{T}\right) \tag{23}$$

The dimensionless discharge is expressed as:

$$Q^* = \frac{Q}{A_u\sqrt{gh_u}} = \frac{Au}{A_u\sqrt{gh_u}} \tag{24}$$

For a triangular channel, the cross sections of the Zones (1) and (2) are similar triangles. The area ratio of the cross sections is equal to the square of the ratio of the corresponding flow depth:

$$\frac{A}{A_u} = \left(\frac{h}{h_u}\right)^2 \tag{25}$$

The dimensionless discharge and the Froude Number are obtained from Eqs. (20, 23–25) as:

$$Q^* = \left(\frac{h}{h_u}\right)^2 \cdot \frac{u}{\sqrt{gh_u}} = \frac{4}{3125}\left(2\sqrt{2} - \frac{X}{T}\right)^4\left(2\sqrt{2} + 4\frac{X}{T}\right) \tag{26}$$

$$F_r = \frac{2\left(1+\sqrt{2}\,\frac{X}{T}\right)}{2\sqrt{2}-\frac{X}{T}} \tag{27}$$

For a triangular channel, the centroid depth for the cross section is one third of the flow depth. Applying this condition for the shock wave, Eq. (16) can be simplified as:

$$\int_0^{h_u}\sqrt{\frac{2}{h}}\mathrm{d}\eta - \int_0^{h_c}\sqrt{\frac{2}{h}}\mathrm{d}\eta = \left[\frac{1}{3}\left(\frac{A_c}{A_d}h_c - h_c - h_d + \frac{A_d}{A_c}h_d\right)\right]^{1/2} \tag{28}$$

Applying the condition that the cross-sectional area of triangular channels is proportional to the square of the depth in the Zones (3) and (4), Eq. (28) is transformed as:

$$\int_0^{h_u}\sqrt{\frac{2}{h}}\mathrm{d}\eta - \int_0^{h_c}\sqrt{\frac{2}{h}}\mathrm{d}\eta = \left[\frac{1}{3}\left(\frac{h_c^3}{h_d^2} - h_c - h_d + \frac{h_d^3}{h_c^2}\right)\right]^{1/2} \tag{29}$$

Integrating Eq. (29) yields:

$$\left(h_c^*\right)^5 - 25\left(h_d^*\right)^2\left(h_c^*\right)^3 + 48\left(h_d^*\right)^2\left(h_c^*\right)^{\frac{5}{2}} - \left(h_d^* + 24\right)\left(h_d^*\right)^2\left(h_c^*\right)^2 + \left(h_d^*\right)^5 = 0 \tag{30}$$

where $h_c^* = h_c / h_u$ =dimensionless water depth in the reach upstream of the shock and $h_d^* = h_d / h_u$ = dimensionless tailwater depth.

The hydraulic characteristic of the Zone 2 is the same as that of the Zone 3 at the junction *N–N* (i.e., rarefaction wave tail). Appling Eqs. (19) and (20) in the junction cross section yields the dimensionless depth and velocity, respectively:

$$h_c^* = \frac{2}{25}\left(2\sqrt{2} - \frac{X_N}{T}\right)^2 \tag{31}$$

$$u_c^* = \frac{u_c}{\sqrt{gh_u}} = \frac{2}{5}\left(\sqrt{2} + 2\frac{X_N}{T}\right) \tag{32}$$

where the subscript "*N*" refers to the junction *N–N*, and X_N is defined by:

$$X_N = \frac{x_N}{h_u} \qquad (3$$

3)

Applying Eq. (31) in Eq. (32) yields:

$$u_c^* = 2\sqrt{2}\left(1-\sqrt{h_c^*}\right) \tag{34}$$

Applying Eq. (34) in Eq. (32) yields the dimensionless location and celerity of the junction *N–N*:

$$X_N = C_2^* T \tag{35}$$

$$C_2^* = \sqrt{2}\left(2-2.5\sqrt{h_c^*}\right) \tag{36}$$

The dimensionless discharge and the Froude Number are expressed as:

$$Q_c^* = 2\sqrt{2}\left(h_c^*\right)^2\left(1-\sqrt{h_c^*}\right) \tag{37}$$

$$F_{rc} = 2\sqrt{2}\left(\frac{1}{\sqrt{h_c^*}}-1\right)$$

(38)

Applying Eq. (34) in Eq. (13) yields the dimensionless wave-front celerity:

$$\xi^* = 2\sqrt{2}\,\frac{\left(h_c^*\right)^2\left(1-\sqrt{h_c^*}\right)}{\left(h_c^*\right)^2-\left(h_d^*\right)^2} \tag{39}$$

The dimensionless shock location is expressed as:

$$X_R = T\xi^* \tag{40}$$

where $X_R = = x_R/h_u$.

Experimental Setup and Flow Measurement Technique

The experiments are performed in a triangular flume of 18 m in length, 1 m width and 1.09 m in height with a horizontal bottom, as shown in Fig. 2. One side wall is vertical for recording the flow with cameras and the slope of the other side wall is 45°. The flume is made of stalinite supported by

a steel frame and is separated by a 15-mm-thick fiberglass plate into two sections with the upstream and the downstream length being 8.37 m and 9.63 m, respectively. The instantaneous dam break is simulated by lifting the plate instantly with an electromagnetic brake asynchronous motor. A new criterion for the maximum plate removal time in non-rectangular channels proposed by Wang et al. (2019) is used:

$$t_{\max} = \sqrt{2h_0 / g} \tag{41}$$

where h_0 = average water depth upstream of the plate, i.e., $h_0 = A_u/B_u$, (A_u and B_u = initially upstream cross-sectional area and water surface width, respectively). Eq. (41) has the same form of the one suggested by Lauber and Hager (1998a) in which h_0 is defined as the upstream water depth. The plate removal time is around 0.1024 s, 0.1250 s and 0.1875 s for the upstream water depth of 0.2 m, 0.4 m and 0.6 m, respectively, satisfying the transient failure condition. A steel gate is located at the downstream end of the channel for providing different wet bed conditions.

To obtain the free surface profiles along the channel and the time evolution of water levels, digital image processing that is based on the camera video of the water flow is used. The digital imaging system contains three parts: a computer, eight high-speed CCD cameras and the MATLAB software (MATLAB 2016) in which camera calibration, frame grab, synchronous images combination and binarization are conducted. The CCD cameras are arranged along the flume and in parallel at the same side of the flume with equal interval of 1.4 m to capture the evolution of the water flow. Cameras are turned on wirelessly by a remote control in order to make cameras work synchronously. Some auxiliary facilities are adopted for ensuring the quality of the video and conveniently applying the image processing technology, such as covering the slopping wall of channel with a smooth white car sticker, dyeing the water with methyl violet, and sheltering the cameras and the channel from the light. The flow measurement includes calibration process and water depth acquisition. Details about the flow measurement adopted in the present experiment can be found in Wang et al. (2019, 2020b). The parameters of total 30 runs are listed in Table 1, which

includes three different initial impoundment depths and ten dimensionless water depths.

Results

Discussion of Analytical Solutions

The dimensionless depth, velocity, discharge and the Froude number against the dimensionless variable *X*/*T* are shown in Fig. 3, in which the analytical solution by Ritter (1892) for rectangular channels is included for comparison. The value of *X*/*T* in the triangular channels ranges from $-\sqrt{2}/2$ to $2\sqrt{2}$, corresponding to $h^* = 1$ and $h^* = 0$ respectively, while it varies from −1 to 2 in rectangular channels. The depth decreases with the increase of *X*/*T*; and the water depth in the triangular channels is overall larger than that in the rectangular channels. The value of water depth is 16/25 and 4/9 at the dam site (i.e., *X*/*T* = 0, *x* = 0) for the triangular and rectangular channels, respectively. The velocity increases with the increase of *X*/*T*. The velocity curves in the two channels intersect with each other at $X/T = 5 - 3\sqrt{2}$ with $u^* = 2\left(2 - \sqrt{2}\right)$. The velocity in the rectangular channels is larger than that in the triangular channels for $X/T < 5 - 3\sqrt{2}$; and the contrary is the case for $X/T > 5 - 3\sqrt{2}$. The discharge increases first and respectively reaches the peak of 0.232 and 0.296 at the dam site for the triangular and rectangular channels, and then decreases with the increase of *X*/*T*. The depth, velocity and discharge in both channels remain constant at the dam site as the time goes by.

It is seen that F_r increases with the increase of *X*/*T*. The Froude number in the triangular and rectangular channels respectively equals to zero at $X/T = -\sqrt{2}/2$ and −1 (corresponding to the location for the leading edge of the rarefaction surge) and respectively equals to one at $X/T = 2\left(\sqrt{2} - 1\right)/\left(2\sqrt{2} + 1\right)$ and *X*/*T* = 0. It is indicated that the transition of flow regime from

subcritical to supercritical in triangular channels takes place downstream of the dam, while it occurs just at the dam site in rectangular channels. F_r approaches infinity at $X/T = 2\sqrt{2}$ and 2 for the triangular and rectangular channel, respectively, corresponding to the front of the leading edge of the positive surge. This won't be true in practice due to the effect of friction.

Fig. 4 presents the profiles of h_c^*, $h_c^* - h_d^*$, u_c^* and Q_c^* against h_d^*, containing the analytical solution by Stoker (1957) for rectangular channels. It is shown from both Eq. (30) and the Stoker's solution that the water depth in Zone 3 (i.e., h_c) is determined only by h_d^*. When the downstream channel bed is initially dry, i.e., $h_d = 0$, it is well known that there is no bore and the water depth in Zone 3 is equal to zero, i.e., $h_c = 0$. Fig. 4 shows that h_c^* increases with the increase of h_d^* and reaches the maximum value of 1 (i.e., $h_c^* = 1$) when the initial water depth downstream is equal to that upstream of a dam, i.e., $h_d^* = 1$. h_c^* in the triangular channels is smaller than that in the rectangular channels; and the difference becomes smaller with increasing h_d^*.

If h_d is larger than zero (i.e. the initial downstream bed is wet), a bore will be formed. The bore height, i.e., the quantity of $h_c - h_d$, is a feature of interest under investigation. When $h_d = 0$, there is no bore and the value of $h_c - h_d$ is equal to zero. The bore height must again approach zero when $h_d = h_u$, i.e., the reservoir head is the same as the tailwater depth. It is seen from Fig. 4 that the dimensionless bore height increases sharply with the increase of h_d^* and respectively reaches the maximum of 0.286 and 0.309 at $h_d^* = 0.230$ and 0.176 in the triangular and rectangular channels; and then gradually decreases to zero at $h_d^* = 1$ (i.e., $h_d = h_u$).

As shown in Fig. 4, the dimensionless velocity in Zone 3, which presents an inverse relation of the dimensionless tailwater depth, decreases sharply for the range of $0 < h_d^* < 0.1$ and then gradually decreases to zero when $h_d^* = 1$. u_c^* with a maximum of $2\sqrt{2}$ at $h_d^* = 0$ in the triangular channels

is larger than that with a maximum of 2 in the rectangular channels.

When $h_d^* = 0$, there is no bore and the discharge Q_c^* in Zone 3 must be zero. On the other hand, when h_c^* approaches the other extreme value, i.e., $h_c^* = 1$, it is indicated from Eq. (37) that Q_c is again equal to zero. Fig. 4 shows that $h_c^* = 1$ when $h_d^* = 1$. Therefore, Q_c must reach a maximum for a certain value of h_d^*. It is seen that Q_c^* increases sharply with the increase of h_d^* and respectively reaches the maximum of 0.232 and 0.296 at $h_d^* = 0.377$ and 0.138 in the triangular and rectangular channels (corresponding to $h_c^* = 16/25$ and 4/9, respectively) and then decreases to zero when $h_d^* = 1$ (corresponding to $h_c^* = 1$).

Table 2 compares the analytical values for special parameters of dam-break flow to visually identify the differences between the hydraulic properties for the triangular and the rectangular channels, including the wave celerities, i.e., C_1^*, C_2^* and ξ^*, which will be further discussed through the comparison with experimental results in the Section "Location and Celerity of Dam-break Wave Front".

Dam-break Wave Evolution

Fig. 5 presents the video images of flow evolution for four tailwater depths with h_u = 0.4 m. On each frame shown in Fig. 5 from top to bottom, the images represent the flow patterns with h_d^* = 0.2, 0.4, 0.6 and 0.8, respectively. The water surface in the reservoir declines when the rarefaction wave front arrives after the dam breaks. It can be seen that the fall of water surface is larger for smaller value of h_d^*. When the tailwater depth is not large (i.e., $h_d^* \leq 0.4$), the water surface profile is characterized by a drop-down curve. For large tailwater depth (i.e., $h_d^* \geq 0.5$), extra negative waves are formed in the reservoir which are originated from the dam site and propagate towards the upstream end due to the tailwater induced resistance force, leading to the undulation of water surface. Comparing with the

experiments of Wang et al. (2019), the inception value of h_d^* for the formation of extra negative waves is smaller in the rectangular channels than that in the triangular channels, i.e., extra negative waves are formed for $h_d^* \geq 0.4$ in the rectangular channels.

Once the gate is removed, the tailwater is pushed by the initial reservoir water flow due to the gravity effect; and the tailwater resists to the drag force. The position of the dam-break wave front falls behind for a given time as the dimensionless tailwater depth h_d^* increases. When the value of h_d^* is very small, the effect of the downstream initial water on the propagation of the dam-break wave is insignificant. For middle value of h_d^* (e.g., h_d^* = 0.2−0.4), a significant interaction between the initial reservoir water and the tailwater is observed. The dam-break wave front is broken, and a jet is formed downstream during the initial stage, which forces the flow to move upward, as seen in the upper two frames in Fig. 5. The jet falls back down the tailwater and produces air entrainment, causing substantial foaming in the free surface of the wave front. This jet-like phenomenon is also observed in the study of Wang et al. (2019), which is quite similar to the behavior of the dam-break flow at the initial stages in the rectangular channels (Stansby et al. 1998; Ozmen-Cagatay and Kocaman 2010; and Kocaman and Ozmen-Cagatay 2015). When h_d^* is large (e.g., h_d^* = 0.6 and 0.8), the jet and the resultant air entrainment are not observed, instead the undular bores are formed, which are similar to the Favre Waves (Favre 1935; Benet and Cunge 1971; Treske 1994; Prüser and Zielke 1994; Soares-Frazão and Zech 2002). The wavelength of the waves increases with the increase of the downstream initial water depth. Accordingly, the frequency of the waves (i.e., the number of waves passing a given cross-section per unit time) decreases as the propagation speed decreases. The time evolutions of dam-break flow with h_u = 0.6 m are similar to those with h_u = 0.4 m.

Water Surface Profiles

Fig. 6 shows the comparison of the measured analytically solved water surface profiles along the channel at t = 0.5 s, 1.0 s, 1.5 s, 2.0 s, 2.5 s, 3.0 s and 3.5 s for different h_d^*. For the sake of clarification, only the water surface profiles in the range of h^* between 0.5 and 1.0 are presented when $h_d^* \geq 0.5$. For $h_d^* \leq 0.4$, both the analytical and experimental results show that the dimensionless water surface profiles in the reservoir at a specific time overlap each other for different tailwater depths; and the effect of h_d^* on the propagation of the rarefaction wave front is insignificant. This may be explained using the analytical model as following. When $h_d^* \leq 0.377$, the junction of Zone 2 and Zone 3 is located at the downstream side of the dam, the shock wave has no influence on the flow upstream of the junction. The prediction of water surface upstream of dam by analytical model reasonably agrees with the measurements except for the rarefaction wave front. It can been seen from the enlarged views that the rarefaction wave front in the experiments moves faster than that predicted by the analytical model. The analytical model shows that the dimensionless water depth at the dam section for $h_d^* \leq 0.377$ is 16/25, which agrees well with the measurements of 0.6–0.7.

Fig. 6 shows the strong dependence of the dam-break flow movement in the reach downstream of the dam on h_d^*. The shock wave front propagates slower when h_d^* is larger. The displacement difference of the shock wave fronts for different values of h_d^* becomes larger with the lapse of time. It is found that the analytical model can well predict the water surface profile after the water rise formed downstream of the dam disappears which cannot be provided by the analytical solution. The wave front predicted by the analytical model is located in front of the measured one, partly due to the omission of bed friction in the analytical model. Such difference between prediction and measurement becomes smaller with the decrease of h_d^*.

Fig. 6 (b) shows that both the measured water surfaces upstream and downstream of the dam

fluctuate around the analytically predicted water surface profiles for $h_d^* \geq 0.5$. It is seen that the measured rarefaction wave front travels faster than that predicted by the analytical model. The position of the shock wave front predicted by the analytical model has better agreement with the measurement for $h_d^* \geq 0.5$ than that for $h_d^* \leq 0.4$. The measured and analytically predicted water surface profiles at t = 0.5–3.5 s for different values of h_d^* with h_u = 0.6 m are similar to those with h_u = 0.4 m.

Time Evolution of Water Level

The stage hydrographs at seven locations (i.e., x = −7, −4, −2, −0.16, 2, 4 and 6 m) are acquired directly from the synchronous recorded images. Fig. 7 shows the comparison of the measured and predicted temporal evolution of water depth at all chosen positions with h_u = 0.4 m. In the reservoir, the rarefaction wave leads to a decline of water level at all locations. When $h_d^* \leq 0.4$, the stage hydrographs for different values of h_d^* at a chosen position are close to each other, which is well captured by analytical model. It is seen that the inception of water level fall predicted by the analytical model is later than that measured, and the lag becomes small towards the dam site. It is shown that the rarefaction wave front provided by the analytical model propagates slower than the measured one. Analytical solution shows that the predicted stage hydrographs collapse in the reservoir region. At the farthest upstream section (x = −7 m), the stage hydrographs predicted by the analytical model deviate from the measurements. The reason is that when the rarefaction wave arrives at the upstream end of channel, sufficient water volume cannot be provided due to the limited reservoir length, resulting in a quick drop of water surface. The inception of deviation takes place earlier at the section that is closer to the upstream end of channel.

The water level downstream of the dam rises quickly as the shock wave arrives and reaches to

a stable state finally. The inception of water level rise is later for larger value of h_d^*, indicating that the shock wave front travels slower with the increase of h_d^*. Both the change of water level over the time and the stable depth are predicted very well by the analytical model, except that the predicted water level has very sharper increase than the measurement at early stage.

When $h_d^* \geq 0.5$, extra negative waves occur in the reservoir, causing the water level undulating over time. The undulation begins earlier for large value of h_d^*. In addition, the undulation amplitude becomes larger towards the dam. The analytical solution shows that the undulation attenuates with the time for a given location and the water level tends to be stable. The undulation of water level is also found in the reach downstream of the dam. For a given location, the inception of undulation takes place later when the value of h_d^* is larger, because the shock wave front propagates slower. Similar to the situation in the reservoir, the attenuation of the undulation with the time is found for a given location and the predicted water level agrees well with the measurements, indicating that the analytical model is able to predict the stable water level in the reaches both the upstream and downstream of the dam.

The measured and analytically predicted temporal evolutions of water depth at all chosen positions with h_u = 0.6 m are similar to those with h_u = 0.4 m.

Location and Celerity of Dam-break Wave Front

Fig. 8 shows the comparison between the measured and analytically predicted locations of shock wave fronts X_R with the time T under different values of h_d^* for three reservoir heads. The time interval of experimental results is 0.5 s. It is shown that the analytical prediction satisfactorily agrees with the measurement for $h_d^* \geq 0.3$, indicating that the shock wave front propagates with an approximately constant speed along the flume. When $h_d^* \leq 0.1$, the variation of X_R with T may be

characterized by a parabolic curve, showing that the wave-front celerity decreases along the flume. A linear relationship is also found between the shock wave-front locations X_R and the time T, as shown in Fig. 8. The wave front moves slower with the increase of the tailwater depth. It is seen that the analytically predicted shock wave front for $h_d^* = 0.0$ moves much faster than the measured shock wave front does. This large difference could be ascribed to the fact that the analytical model ignores bed friction, which plays an important role for small h_d^*. Fig. 8 also shows that the effect of h_d^* on the shock wave front weakens with the increase of h_d^*.

Fig. 9 shows the comparison of the predicted and measured locations of the rarefaction wave tail (i.e., X_N) with the time T for different h_d^* and three reservoir heads. It is seen that the analytical model can provide good results when $h_d^* \geq 0.3$. It is obtained from Eq. (36) that when $h_c^* = 16/25$, corresponding to $h_d^* = 0.377$, the rarefaction wave tail is located at the dam site (i.e., X_N = 0), indicating that the rarefaction wave tail is observed in the downstream reach of the dam for h_d^* < 0.377 and occurs in the reservoir for h_d^* > 0.377. The analytical model is well validated with the measurements. For the rectangular channel, the location of the rarefaction wave tail at the dam site requires a smaller tailwater depth, i.e., $h_d^* = 0.138$, corresponding to $h_c^* = 4/9$.

Fig. 10 shows the comparison between the measured and analytically predicted locations of rarefaction wave fronts X_M with the time T for different h_d^* and three reservoir heads. The analytical model provides rarefaction wave front propagation with a constant speed, which is independent of the tailwater level. Fig. 10 shows that the analytical model slightly underestimates the location of rarefaction wave front when h_d^* < 0.4 and provides good prediction for $h_d^* \geq 0.4$.

Fig. 11 presents the dimensionless celerity of rarefaction wave front, rarefaction wave tail and shock wave front against the dimensionless tailwater depth h_d^*, in which the analytical solution by

Stoker (1957) for the rectangular channel is included for comparison. For a given h_d^*, the experimental celerities will be approximated by the steady values which are equal to the celerities at x = –7.5 m and 7.5 m for the rarefaction wave front and the shock wave front, respectively. The dimensionless distances from the dam site are X = ±37.5, ±18.75, ±12.5 for h_u = 0.2 m, 0.4 m, 0.6 m, respectively. It is seen that the predicted rarefaction wave front propagates with a constant speed of $C_1^* = -\sqrt{2}/2$, which is slightly slower than the measured celerity of the rarefaction wave front when h_d^* < 0.4, while the predicted C_1^* agrees well with the measurements for h_d^* ≥ 0.4. It is also shown that the tailwater depth has insignificant effects on the movement of the rarefaction wave front. The curve of $C_1^* = -1$ for the rectangular channel is under the one in the triangular channel, indicating that the rarefaction wave front travels faster in the former channel.

Both the analytical prediction and measurement show that C_2^* decreases rapidly as h_d^* ranges from 0 to 0.2, and then gradually decreases with the increase of h_d^*. It is seen that the analytical model accurately predicts the propagation speed of the rarefaction wave tail (i.e., C_2^*) when h_d^* ≥ 0.3 and slightly over-predicts the speed for h_d^* < 0.2. When h_d^* = 0, the measured C_2^* (approximate 1.6) has the identical value as the shock wave front celerity ξ^*, and is smaller than the analytical prediction of $2\sqrt{2}$. It can be seen that the analytical prediction for the shock wave front celerity agrees well with the measurement when the value of h_d^* is larger than 0.2. The curve for the analytical solution of C_2^* in the rectangular channel drops from 2 to –1 throughout the entire range of h_d^*, intersecting with the x axis at $h_d^* = 0.138$ for which the rarefaction wave tail is located in the dam site. The shock wave front celerity ξ^* decreases monotonically from $2\sqrt{2}$ to $\sqrt{2}/2$ in the entire range of h_d^* in the triangular channel, while it drops from 2 to the minimum of 0.936 at $h_d^* = 0.349$ and then grows slowly to 1 in the rectangular channel. The curves of ξ^* intersect with

each other at $h_d^* = 0.281$ with $\xi^* = 0.938$. The value of ξ^* in the triangular channel is larger than that in the rectangular channel for $h_d^* < 0.281$, and the contrary is true for $h_d^* > 0.281$. The dimensionless celerities for three different initial reservoir depths are close at the same value of h_d^* for both C_2^* and ξ^*. However, the measured C_1^* at h_u = 0.6 m slightly deviates from those under h_u = 0.2 m and 0.4 m. The reason is that C_1^* decreases with the distance and tends to reach a steady value, while the steady state for C_1^* under h_u = 0.6 m is not reached due to the limited reservoir length.

Conclusions

In the present study, an analytical model that is based on the method of characteristics, has been developed for the instantaneous dam-break floods down a horizontal and frictionless channel with a triangular cross-section. The variation of the dimensionless water depth h^*, velocity u^* and discharge Q^*, and the Froude number with the dimensionless variable X/T has been discussed. The variation of dimensionless depth h_c^*, bore height $h_c^* - h_d^*$, velocity u_c^*, discharge Q_c^*, and the Froude number in Zone 3, and wave-front celerities (i.e., C_1^*, C_2^*, ξ^*) against h_d^* is investigated. Laboratory experiments of dam-break flows have been conducted in a prismatic, horizontal, triangular and smooth flume, covering a wide range of initial reservoir heads and tailwater levels. Digital image processing, which is a non-intrusive flow measurement technique, is adopted in the experiments to provide the temporal evolution of the free surface profiles along the whole channel. The analytical model is well validated using the laboratory measurements. The comparisons between the analytical results and the well-known solutions by Ritter (1892) and Stoker (1957) for rectangular channels are also presented. The following conclusions can be drawn:

(1) When the tailwater depth is not large (i.e., $h_d^* \leq 0.4$), the dimensionless water surface profiles in the reservoir for different h_d^* are characterized by drop-down curves, which overlap each other at some specific time. The tailwater depth has insignificant influence on the rarefaction wave propagation. The analytical model shows satisfactory agreement with the measured water surface profile upstream of the dam, though the predicted rarefaction wave front is slightly slower than the measured one. The analytical solution for the dimensionless water depth at the dam section is 16/25, which is within the range of around 0.6–0.7 measured in the tests. It is found that the dependence of the movement of dam-break flows downstream of the dam on the tailwater depth is strong. The shock wave front propagates slower for larger value of h_d^* and the displacement difference of shock wave fronts for different h_d^* becomes larger with time.

(2) When the tailwater depth is sufficiently large (i.e., $h_d^* \geq 0.5$), there are extra negative waves generated in the reservoir, leading to the undulations of water surface whose profile is related to the value of h_d^*. In the downstream reach, a rise of water surface is found close to the dam and becomes weaker for larger value of h_d^*. Such water rise will evolve into undulations in the end. The analytical model can provide a stable value for the undulations and is not able to predict the varying undulations. For the same value of h_d^*, the dam-break flow evolutions and the water surface profiles under different reservoir heads remain similar. The significant discrepancy is that the fronts of dam-break waves (i.e., rarefaction waves, extra negative waves and shock waves) propagate faster for a larger reservoir head, resulting in an earlier inception for the changes of water surfaces both in the reservoir and the downstream reach.

(3) The profiles of h^*, u^*, Q^* and Fr along X/T as well as the variations of h_c^*, $h_c^* - h_d^*$, u_c^* and Q_c^* against h_d^* in the triangular channel are found similar to those in the rectangular channel.

h^* decreases monotonically, while u^* and Fr increases in the whole range of X/T. Q^* increases first to the peak at the dam site and then declines to zero. The depth, velocity and discharge at the dam site keep invariant with time. h_c^* increases from zero to one with increasing h_d^*, while u_c^* drops from the maximum to zero. Both $h_c^* - h_d^*$ and Q_c^* increase sharply to the peak and then fall down to zero at $h_d^* = 0$. The rarefaction wave front propagates upstream with a constant speed, while the celerity of the rarefaction wave tail drops downstream of the dam and increases in the reservoir with h_d^*.

(4) The differences between the hydraulic properties in the two channels are also identified analytically, which should be related to the discrepancy in the hydraulic ratio of channels. The range of X/T is between $-\sqrt{2}/2$ and $2\sqrt{2}$ in the triangular channels, while it varies from −1 to 2 in the rectangular channels. h^* in the triangular channels are overall larger than those in the rectangular channels and the contrary is true for Fr. The value of u^* in the rectangular channels is larger than that in the triangular channels for $X/T < 5-3\sqrt{2}$; and the contrary is the case for $X/T > 5-3\sqrt{2}$. The peaks of Q^* are 0.232 and 0.296 for the triangular and rectangular channels, respectively.

(5) h_c^* in the triangular channels is smaller than that in the rectangular channels, while the contrary is the case for u_c^*. The peak of $h_c^* - h_d^*$ are 0.286 and 0.309 and the maximum of Q_c^* equals 0.232 and 0.296 in the triangular and rectangular channels, respectively. The rarefaction wave front with $C_1^* = -\sqrt{2}/2$ in the triangular channels travels slightly slower than that with $C_1^* = -1$ for the rectangular channels. The rarefaction wave tail with C_2^* for the triangular channels moves faster than that for the rectangular channels in the reach downstream of the dam, and the contrary is true in the reservoir. h_d^* respectively equals 0.377 and 0.138 in the triangular and rectangular channels for $C_2^* = 0$, which serves as a criterion for determining if the tailwater affects the

hydraulics upstream of the dam. ξ^* presents a monotonic decrease from $2\sqrt{2}$ to $\sqrt{2}/2$ in the triangular channels, while it shows a sharp drop from 2 to the minimum of 0.936 followed by a slow growth to 1 in the rectangular channels. The shock wave front in the triangular channels propagates faster than that in the rectangular channels for $h_d^* < 0.281$, and the contrary is true for $h_d^* > 0.281$.

(6) The analytical model accurately predicts the effect of the initial downstream water depth on the propagation of flood waves generated by the dam break in the triangular channels. The laboratory data generated in this study with a wide range of tailwater depth could be useful for researchers to validate their analytical and numerical models of dam-break flows.

Data Availability Statement

Some or all data, models, or code generated or used during the study are available from the corresponding author by request (including analytical and experimental test data).

Acknowledgements

This study is supported by the National Natural Science Foundation of China (Grant No: 51879179), Sichuan Science and Technology Program (No. 2019JDTD0007) and Open Fund from the State Key Laboratory of Hydraulics and Mountain River Engineering, Sichuan University (SKHL1809).

Notation

The following symbols are used in this paper:

A = cross-sectional area;

B = water surface width;

C_1 = rarefaction wave front celerity;

C_2 = rarefaction wave tail celerity;

F_r = Froude Number;

g = gravity acceleration;

h = flow depth;

h_0 = average water depth upstream of the plate, $h_0 = A_u/B_u$;

$\bar{h}$ = centroid water depth;

Q = flow discharge;

T = dimensionless time, $T = t(g/h_u)^{1/2}$;

t = time;

t_{max} = maximum plate removal time for simulating instantaneous dam break;

u = flow mean velocity;

X = dimensionless distance along flow direction originated from the dam site, $X = x/h_u$;

x = distance along flow direction originated from dam site;

η = variable of integration; and

ξ = shock wave-front celerity.

Superscripts

* = dimensionless quantity.

Subscripts

c = reach upstream of the shock;

d = reach downstream of the shock;

M = position of rarefaction wave front;

N = position of rarefaction wave tail;

R = location of shock wave-front; and

u = undisturbed upstream reach.

References

Ancey, C., R. M. Iverson, M. Rentschler, and R. P. Denlinger. 2008. "An exact solution for ideal dam-break floods on steep slopes." *Water Resour. Res*. 44(1): 567–568. https://doi.org/10.1029/2007WR006353

Aureli, F., A., Maranzoni, and P., Mignosa. 2014. “A semi-analytical method for predicting the outflow hydrograph due to dam-break in natural valleys.” *Adv. Water Resour*. 63: 38–44. http://dx.doi.org/10.1016/j.advwatres.2013.11.001

Bellos, C. V., J. V. Soulis, and J. G. Sakkas. 1992. “Experimental investigation of two-dimensional dam-break induced flows.” *J. Hydraul. Res*. 30 (1): 47–63. https://doi.org/10.1080/00221689209498946

Benet, F., and J. A. Cunge. 1971. “Analysis of experiments on secondary undulations caused by surge waves in trapezoidal channels.” *J. Hydraul. Res*. 9(1): 11–33. DOI: 10.1080/00221687109500335

Bukreev, V. I., and A. V. Gusev. 2005. “Initial stage of the generation of dam-break waves.” *Doklady Phys*. 50 (4): 200–203. https://link.springer.com/article/10.1134/1.1922561

Chanson, H. 2009. “Application of the method of characteristics to the dam break wave problem.” *J. Hydraul. Res*. 47(1): 41–49. https://doi.org/10.3826/jhr.2009.2865

Chen, H. Y., W. L. Xu, J. Deng, Y. Xue, and J. Li. 2013. “Experimental investigation of pressure load exerted on a downstream dam by dam-break flow.” *J. Hydraul. Eng*. 140 (2): 199–207. https://doi.org/10.1061/(ASCE)HY.1943-7900.0000743

Chen, Y. L., C. Wu, and B. Wang. 2011. “Similarity solution of dam-break flow on horizontal frictionless channel.” *J. Hydraul. Res*. 49(3): 384–387. https://doi.org/10.1080/00221686.2011.571537

Chow, V. T. 1959. *Open channel hydraulics*. New York: McGraw-Hill.

Dressler, R. F. 1952. “Hydraulic resistance effect upon the dam-break functions.” *J. Res. Natl. Bur. Stand*. 49(3): 217–225.

Dressler, R. F. 1954. “Comparison of theories and experiments for the hydraulic dam-break wave.” *in Proc. Int. Assoc. Scientific Hydrology Assemblée Générale Rome*. 3(38): 319-328.

Escoffier, F. F., and M. B. Boyd. 1962. “Stability aspects of flow in open channel.” *In: Proceedings*

ASCE, vol. 88(NY6): 145–66.

Favre, H. 1935. *Etude théorique et expérimentale desondes de translation dans les canaux découverts*. Dunod, Paris.

Fernandez-Feria, R. 2006. “Dam-break flow for arbitrary slopes of the bottom.” *J. Eng. Math*. 54(4): 319–331. DOI:10.1007/s10665-006-9034-5

Fraccarollo, L., and E. F. Toro. 1995. “Experimental and numerical assessment of the shallow water model for two-dimensional dam-break type problems.” *J. Hydraul. Res*. 33 (6): 843–864. https://doi.org/10.1080/00221689509498555

Henderson, F. M. 1966. *Open channel flow*. New York: MacMillan.

Hogg, A. J. 2006. “Lock-release gravity currents and dam-break flows.” *J. Fluid Mech*. 569: 61–87. https://doi.org/10.1017/S0022112006002588

Hunt, B. 1982. “Asymptotic solution for dam-break problems.” *J. Hydraul. Div*. 108(1): 115–126.

Hunt, B. 1983. “Asymptotic solution for dam break on sloping channel.” *J. Hydraul. Eng*. 109(12): 1698–1706. https://doi.org/10.1061/(ASCE)0733-9429(1983)109:12(1698)

Hunt, B. 1984. “Perturbation solution for dam-break floods.” *J. Hydraul. Eng*. 110(8): 1058–1071. https://doi.org/10.1061/(ASCE)0733-9429(1984)110:8(1058)

Katopodes, N. D., and D. R. Schamber. 1983. “Applicability of dam-break flood wave models.” *J. Hydraul. Eng*. 109(5): 702–721. https://doi.org/10.1061/(ASCE)0733-9429(1983)109:5(702)

Katopodes, N. D., and T. Strelkoff. 1978. “Computing two-dimensional dam-break flood waves.” *J. Hydraul. Div*. 104(9): 1269–1288.

Kocaman, S., and H. Ozmen-Cagatay. 2015. “Investigation of dam-break induced shock waves impact on a vertical wall.” *J. Hydrol*. 525: 1–12. https://doi.org/10.1016/j.jhydrol.2015.03.040

LaRocque, L., J. Imran, and M. Chaudhry. 2013. “Experimental and numerical investigations of two-dimensional dam-break flows.” *J. Hydraul. Eng*. 139(6): 569–579. https://doi.org/10.1061/(ASCE)HY.1943-7900.0000705

Lauber, G., and W. H. Hager. 1998a. “Experiments to dambreak wave: horizontal channel.” *J. Hydraul. Res*. 36(3): 291-307. https://doi.org/10.1080/00221689809498620

Lauber, G., and W. H. Hager. 1998b. “Experiments to dambreak wave: sloping channel.” *J. Hydraul. Res*. 36(5): 761-773. https://doi.org/10.1080/00221689809498601

Liu, W. J., B. Wang, Y. L. Chen, C. Wu, and X. Liu. 2018. “Assessing the analytical solution of one-dimensional gravity wave model equations using dam-break experimental measurements.” *Water*. 10(9): 1261. https://doi.org/10.3390/w10091261

Liu, W. J., B. Wang, J. M. Zhang, Y. L. Chen, C. Wu, X. Liu, and J. J. Song. 2019. “Experimental study on dam-break flow under different upstream and downstream initial water depth.” *Advanced Engineering Sciences*. 51(2): 1–9 (in Chinese). doi:10.15961/j.jsuese.201800374

Mangeney, A., P. Heinrich, and R. Roche. 2000. “Analytical solution for testing debris avalanche numerical models.” *Pure Appl. Geophys*. 157: 1081–1096.

Miller, S., and M. H. Chaudhry. 1989. “Dam-break flows in curved channel.” *J. Hydraul. Eng*. 115(11): 1465–1478. https://doi.org/10.1061/(ASCE)0733-9429(1989)115:11(1465)

Oertel, M., and D. B. Bung. 2012. “Initial stage of two-dimensional dam-break waves: laboratory versus VOF.” *J. Hydraul. Res*. 50(1): 89–97. https://doi.org/10.1080/00221686.2011.639981

Ozmen-Cagatay, H., and S. Kocaman. 2010. “Dam-break flows during initial stage using SWE and RANS approaches.” *J. Hydraul. Res*. 48 (5): 603–611. https://doi.org/10.1080/00221686.2010.507342

Ozmen-Cagatay, H., and S. Kocaman. 2012. “Investigation of dam-break flow over abruptly contracting channel with trapezoidal-shaped lateral obstacles.” *J. Fluids Eng*. 134(8): 081204. doi:10.1115/1.4007154

Ozmen-Cagatay, H., S. Kocaman, and H. Guzel. 2014. “Investigation of dam-break flood waves in a dry channel with a hump.” *J. Hydro-environ. Res*. 8: 304–315. https://doi.org/10.1016/j.jher.2014.01.005

Prüser, H. H., and W. Zielke. 1994. “Undular bores (Favre Waves) in open channels theory and numerical Simulation.” *J. Hydraul. Res*. 32(3): 337–354. http://dx.doi.org/10.1080/00221689409498737

Ritter, A. 1892. “Die Fortpflanzung der Wasserwellen.” *Z. Ver. Dtsch. Ing*. 36(33): 947–954 (in German).

Sakkas, J. G., and T. Strelkoff. 1973. “Dam-break flood in a prismatic dry channel.” *J. Hydraul. Div*. 99(12): 2195–2216.

Sakkas, J. G., and T. Strelkoff. 1976. “Dimensionless solution of dam-break flood waves.” *J. Hydraul. Div*. 102(2): 171–184.

Schamber, D. R., and N. D. Katopodes. 1984. “One-dimensional models for partially breached dams.” *J. Hydraul. Eng*. 110(8): 1086–1102. https://doi.org/10.1061/(ASCE)0733-9429(1984)110:8(1086)

Soares-Frazão, S. S., and Y. Zech. 2002. “Undular bores and secondary waves–Experiments and hybrid finite-volume modeling.” *J. Hydraul. Res*. 40(1): 33–43. https://doi.org/10.1080/00221680209499871

Soares-Frazão, S. S., and Y. Zech. 2007. “Experimental study of dam-break flow against an isolated obstacle.” *J. Hydraul. Res*. 45: 27–36 (Extra issue). https://doi.org/10.1080/00221686.2007.9521830

Stansby, P., A. Chegin, and T. Barnes. 1998. “The initial stages of dam-break flow.” *J. Fluid Mech*. 374: 407–424. doi:10.1017/S0022112098009975

Stoker, J. J. 1957. *Water waves: The mathematical theory with applications*. Interscience, New York.

Su, S. T., and A. H. Barnes. 1970. “Geometric and frictional effects on sudden release.” ASCE J. Hydraul. Div. 96(11): 2185–2200.

MATLAB. 2016. *Camera calibrator help*. The MathWorks, Inc.

Treske, A. 1994. “Undular bores (favre-waves) in open channels - Experimental studies.” *J. Hydraul.*

Res, 32(3): 355−370.

Wang, B., Y. L. Chen, C. Wu, Y. Peng, X. Ma, and J. J. Song. 2017. "Analytical solution of dam-break flood wave propagation in a dry sloped channel with an irregular-shaped cross-section." *J. Hydro-environ. Res*. 14: 93–104. http://dx.doi.org/10.1016/j.jher.2016.11.003

Wang, B., J. M. Zhang, Y. L. Chen, Y. Peng, X. Liu, and W. J. Liu. 2019. "Comparison of measured dam-break flood waves in triangular and rectangular channels." *J. Hydrol*. 575: 690–703. https://doi.org/10.1016/j.jhydrol.2019.05.081.

Wang, B., Y. L. Chen, Y. Peng, J. M. Zhang, and Y. K. Guo. 2020a. "Analytical solution of shallow water equations for ideal dam-break flood along a wet bed slope." *J. Hydraul. Eng*. 146(2): 06019020. https://doi.org/10.1061/(ASCE)HY.1943-7900.0001683.

Wang, B., W. J. Liu, W. Wang, J. M. Zhang, Y. L. Chen, Y. Peng, X. Liu, and S. Yang. 2020b. "Experimental and numerical investigations of similarity for dam-break flows on wet bed." *J. Hydrol*. 583: 124598. https://doi.org/10.1016/j.jhydrol.2020.124598.

Whitham, G. B. 1955. "The effects of hydraulic resistance in the dam-break problem." *Proc. R. Soc. London*. 227(1170): 399–407.

Wu, C., G. Q. Dai, and C. G. Wu. 1993. "Model of dam-break floods for channels of arbitrary cross section." *J. Hydraul. Div*. 119(8): 911–923. https://doi.org/10.1061/(ASCE)0733-9429(1993)119:8(911)

Wu, C., G. F. Huang, and Y. H. Zheng. 1999. "Theoretical solution of dam-break shock wave." *J. Hydraul. Eng*. 125(11): 1210–1215. https://doi.org/10.1061/(ASCE)0733-9429(1999)125:11(1210)

Zanuttigh, B., and A. Lamberti. 2011. "Dam-break waves in power-law channel section." *J. Hydraul. Eng*. 127(4): 322–326. https://doi.org/10.1061/(ASCE)0733-9429(2001)127:4(322)

Figure captions list

Fig. 1. Definition sketch for dam-break waves.

Fig. 2. Experimental set up.

Fig. 3. Profiles of dimensionless depth, velocity, discharge and Froude number against X/T.

Fig. 4. Profiles of h_c^*, $h_c^* - h_d^*$, u_c^* and Q_c^* against h_d^*.

Fig. 5. Experimental images of the flow for h_d^* = 0.2, 0.4, 0.6 and 0.8 with h_u = 0.4 m (a) in the reservoir; (b) in the downstream flume.

Fig. 6. Comparison of the measured and predicted dimensionless water depth with h_u = 0.4 m for (a) h_d^* = 0.1, 0.2, 0.3 and 0.4; (b) h_d^* = 0.5, 0.6, 0.7, 0.8 and 0.9.

Fig. 7. Comparison of the measured and analytically predicted stage hydrographs at different positions with h_u = 0.4 m for (a) h_d^* = 0.1, 0.2, 0.3 and 0.4; (b) h_d^* = 0.5, 0.6, 0.7, 0.8 and 0.9.

Fig. 8. Comparison of the measured and predicted locations of shock wave fronts.

Fig. 9. Comparison of the measured and predicted locations of rarefaction wave tails.

Fig. 10. Comparison of the measured and predicted locations of rarefaction wave fronts.

Fig. 11. Comparison of the measured and predicted C_1^*, C_2^* and ξ^*.

Table captions list

Table 1. Test conditions.

Table 2. Special parameter values of dam-break flow for triangular and rectangular channels.

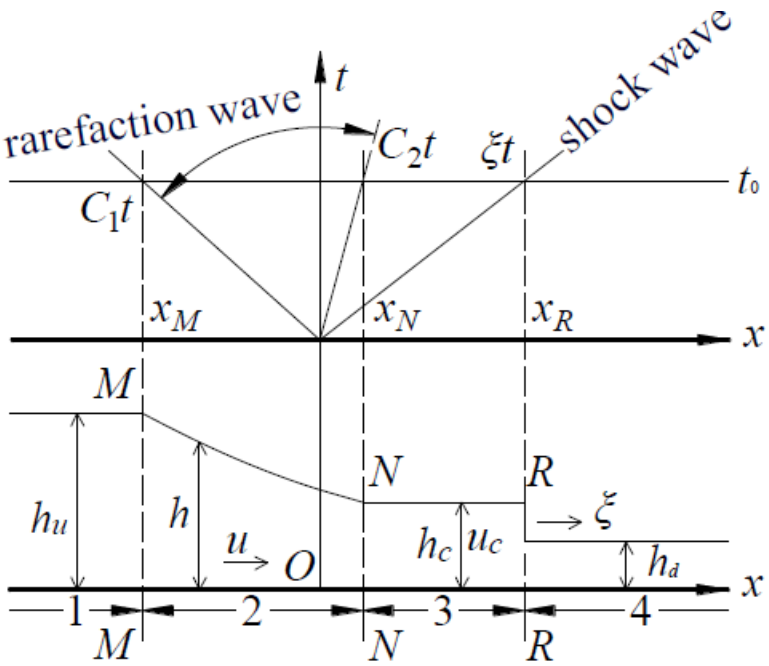

Fig. 1. Definition sketch for dam-break waves.

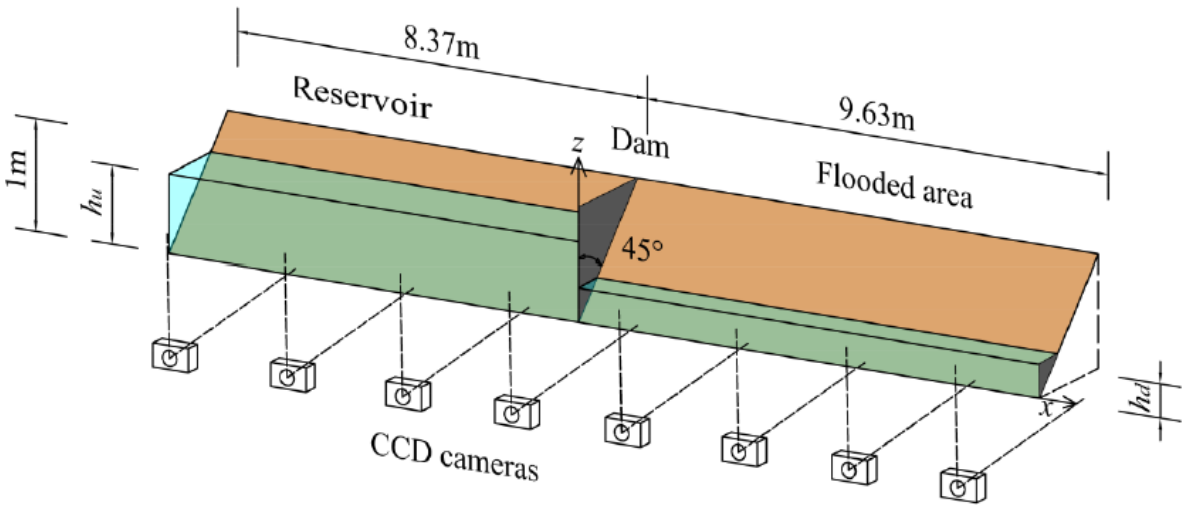

Fig. 2. Experimental set up.

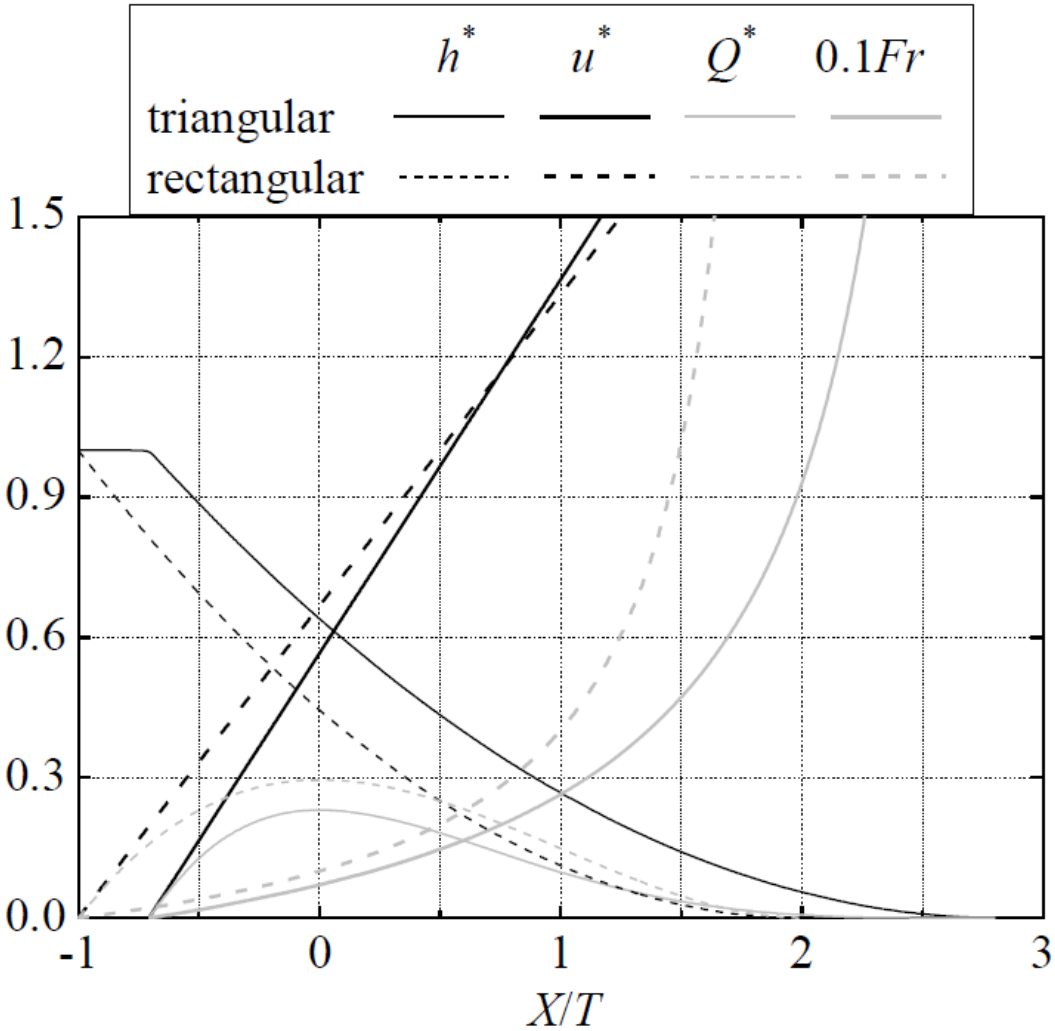

Fig. 3. Profiles of dimensionless depth, velocity, discharge and Froude number against X/T

721

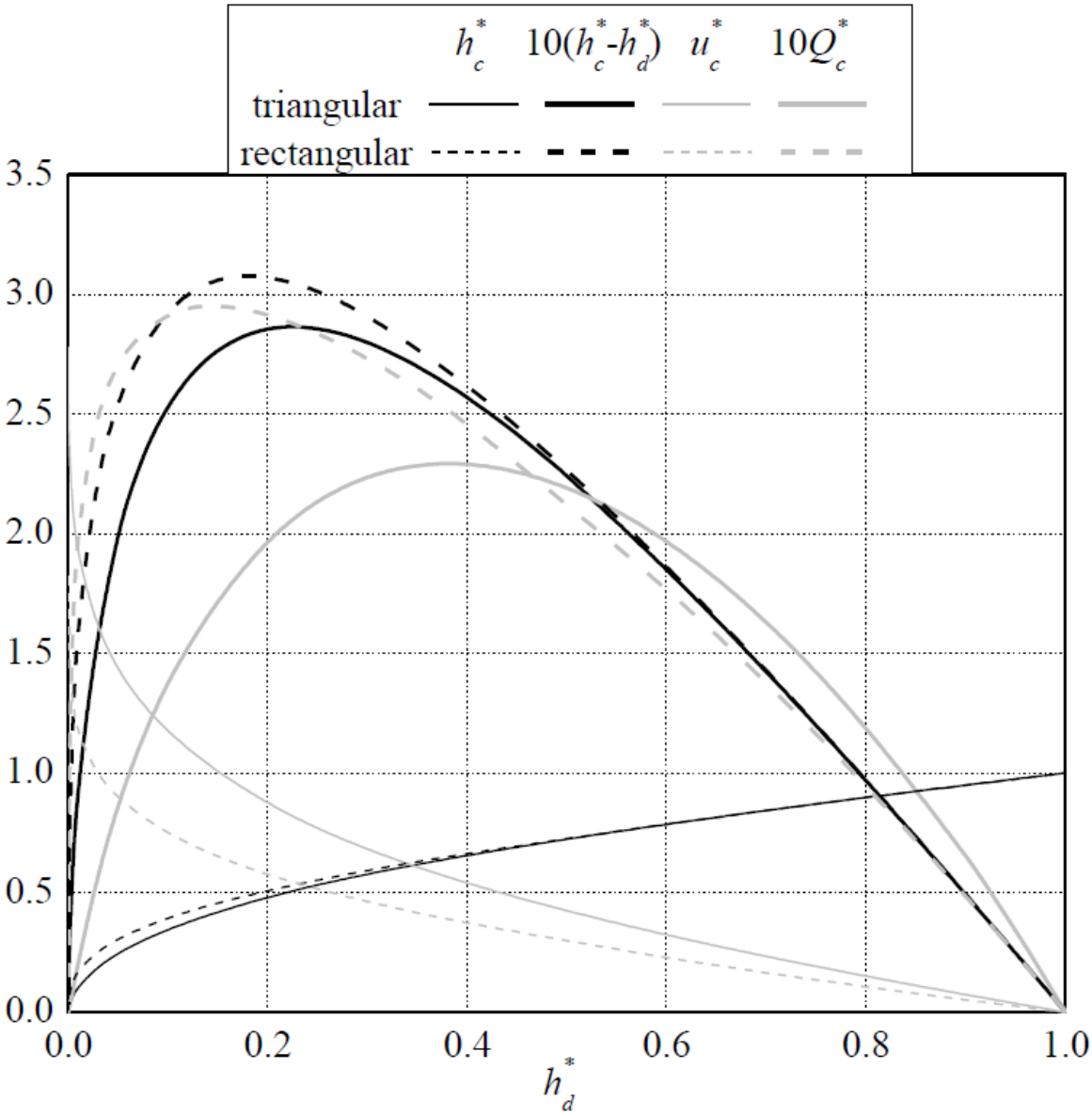

Fig. 4. Profiles of h_c^*, $h_c^* - h_d^*$, u_c^* and Q_c^* against h_d^*.

722

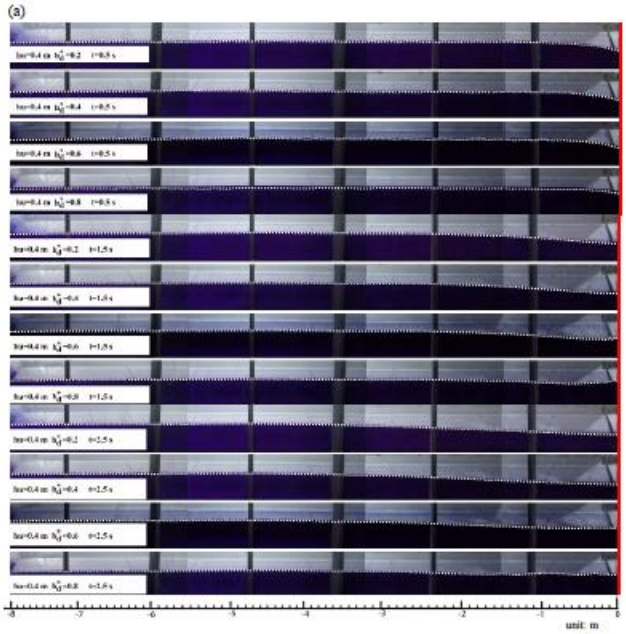

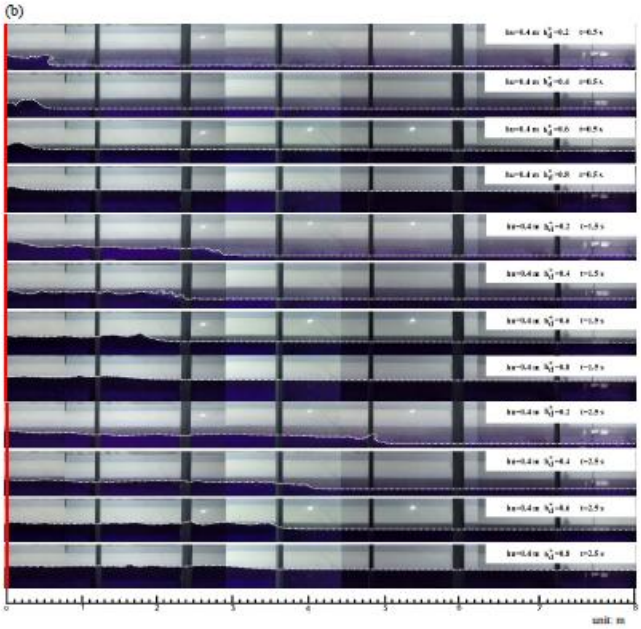

Fig. 5. Experimental images of the flow for h_d^* = 0.2, 0.4, 0.6 and 0.8 with h_w = 0.4 m (a) in the reservoir; (b) in the downstream flume. The dam site is indicated with red lines.

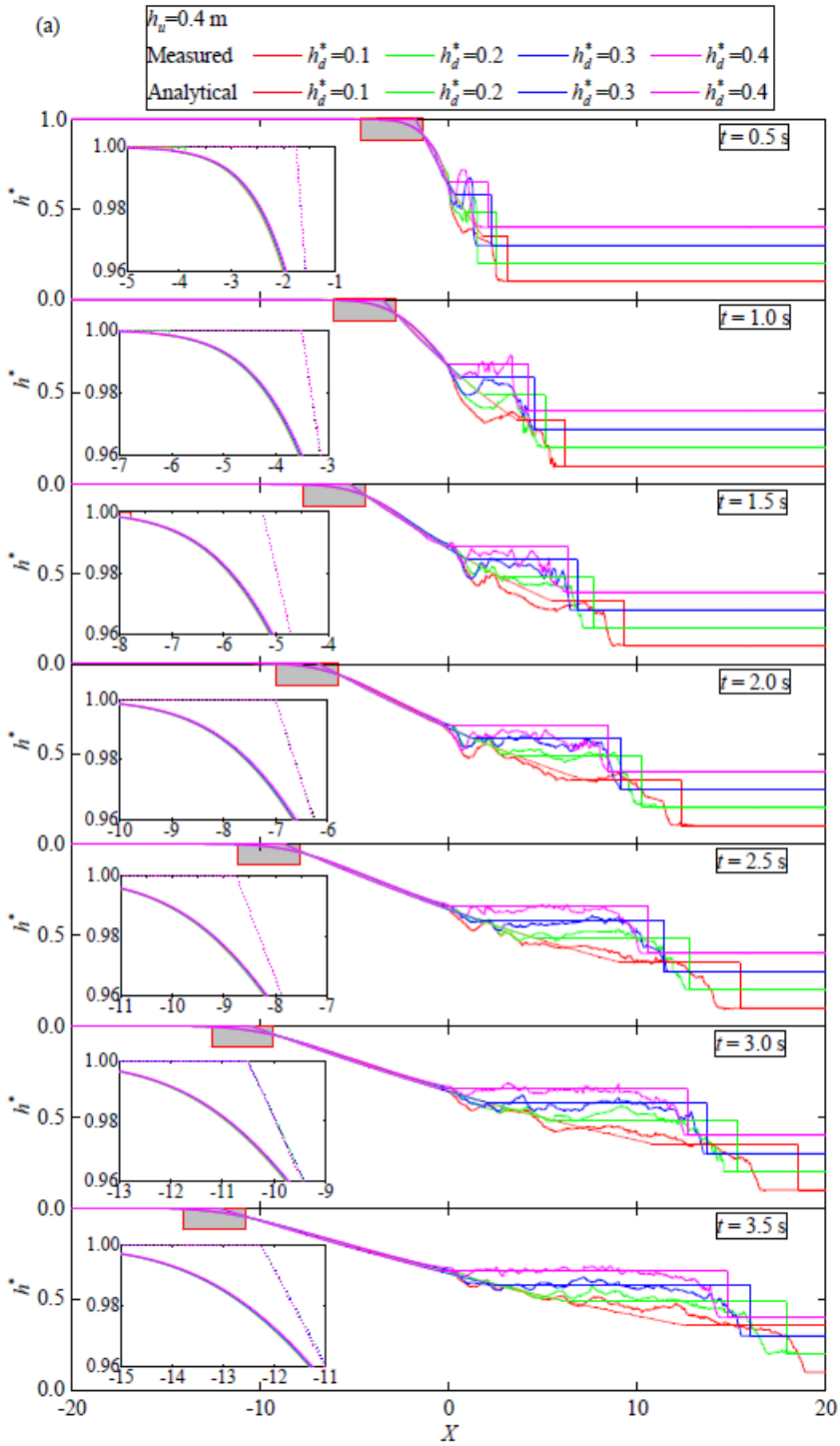
(a)
h_u=0.4 m
Measured h_d^*=0.1 h_d^*=0.2 h_d^*=0.3 h_d^*=0.4
Analytical h_d^*=0.1 h_d^*=0.2 h_d^*=0.3 h_d^*=0.4
t = 0.5 s
t = 1.0 s
t = 1.5 s
t = 2.0 s
t = 2.5 s
t = 3.0 s
t = 3.5 s
h^*
X

725

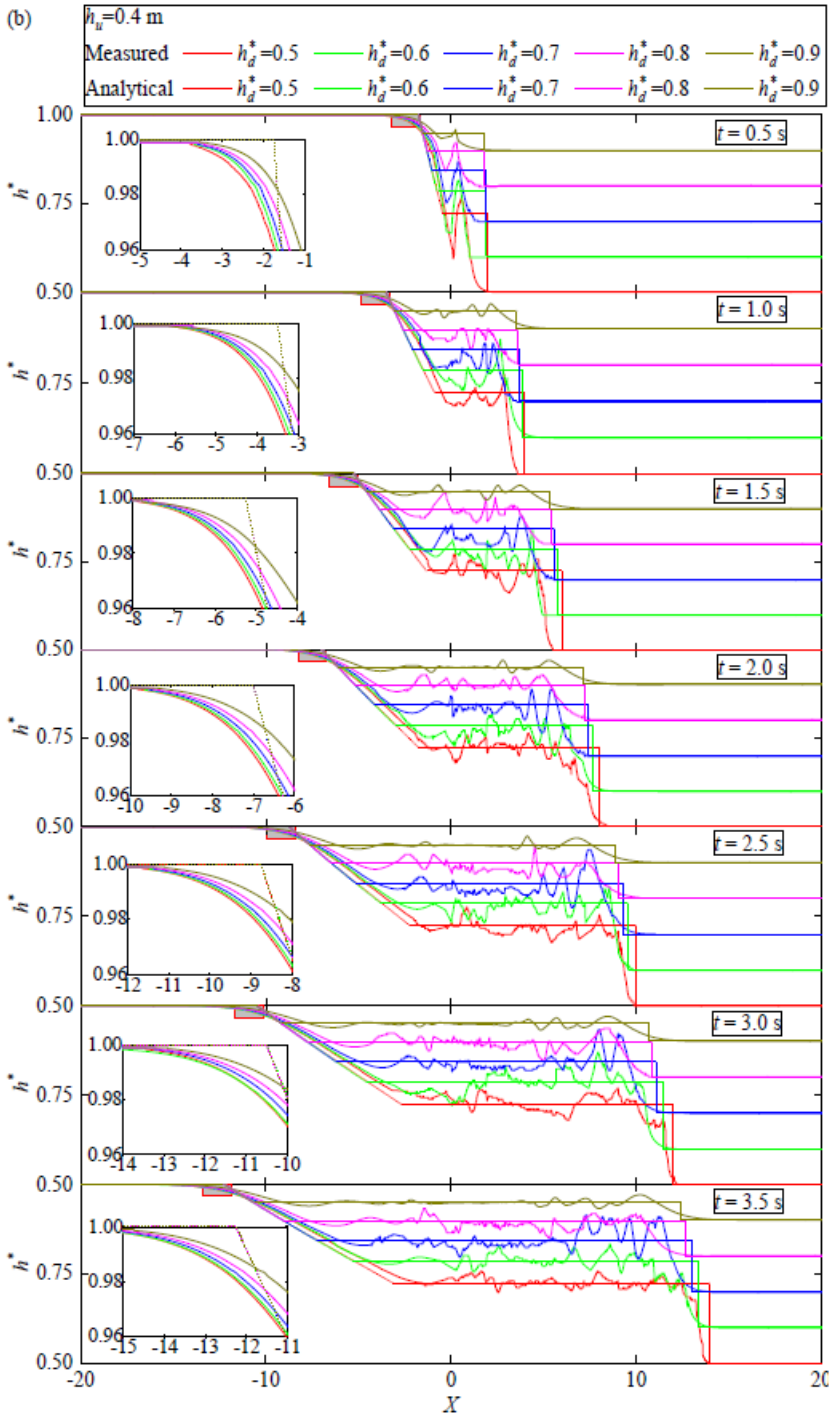

Fig. 6. Comparison of the measured and predicted dimensionless water depth with h_u = 0.4 m for (a) h_d^* = 0.1, 0.2, 0.3 and 0.4; (b) h_d^* = 0.5, 0.6, 0.7, 0.8 and 0.9.

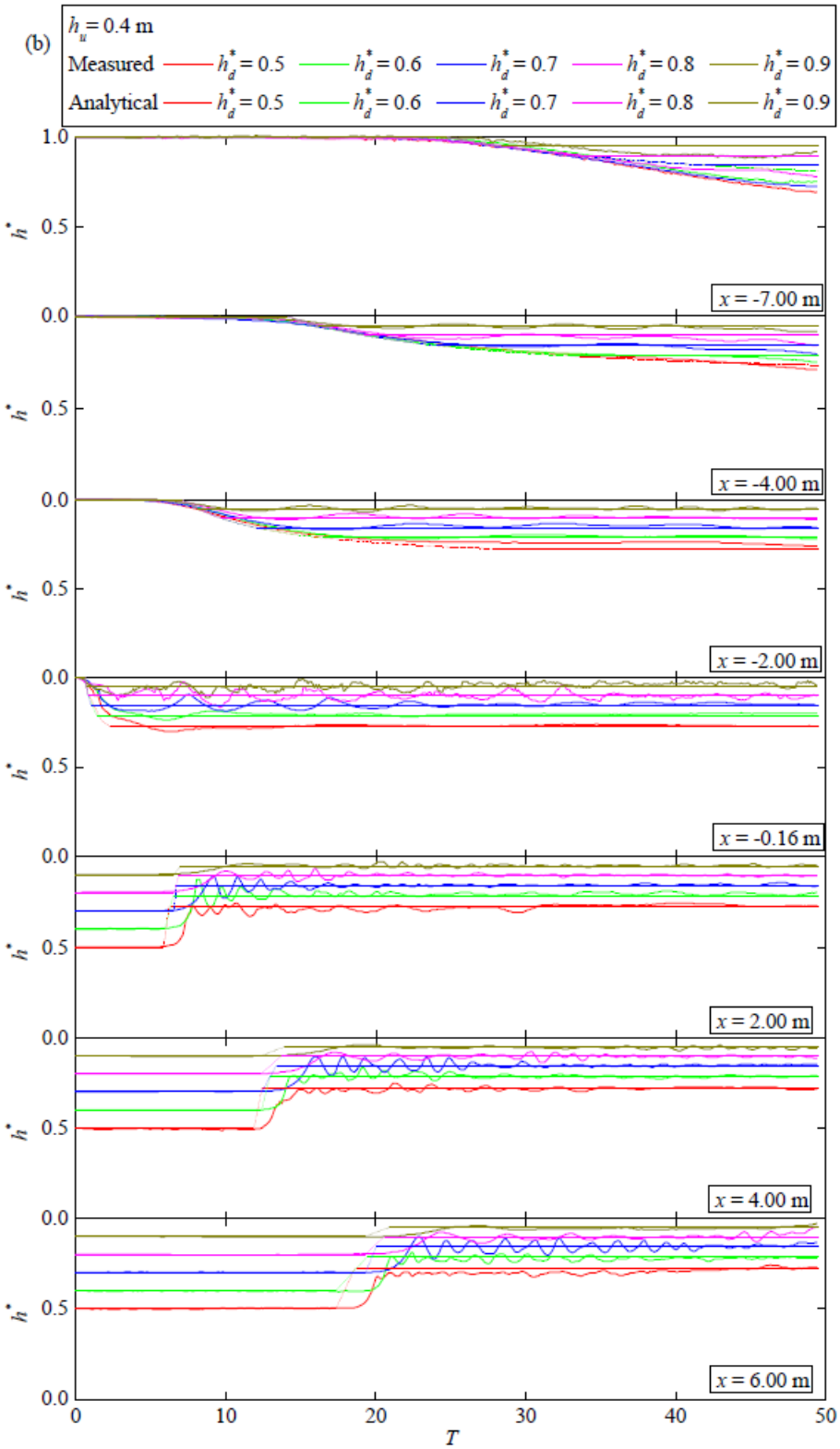

Fig. 7. Comparison of the measured and analytically predicted stage hydrographs at different positions with h_u = 0.4 m for (a) h_d^* = 0.1, 0.2, 0.3 and 0.4; (b) h_d^* = 0.5, 0.6, 0.7, 0.8 and 0.9.

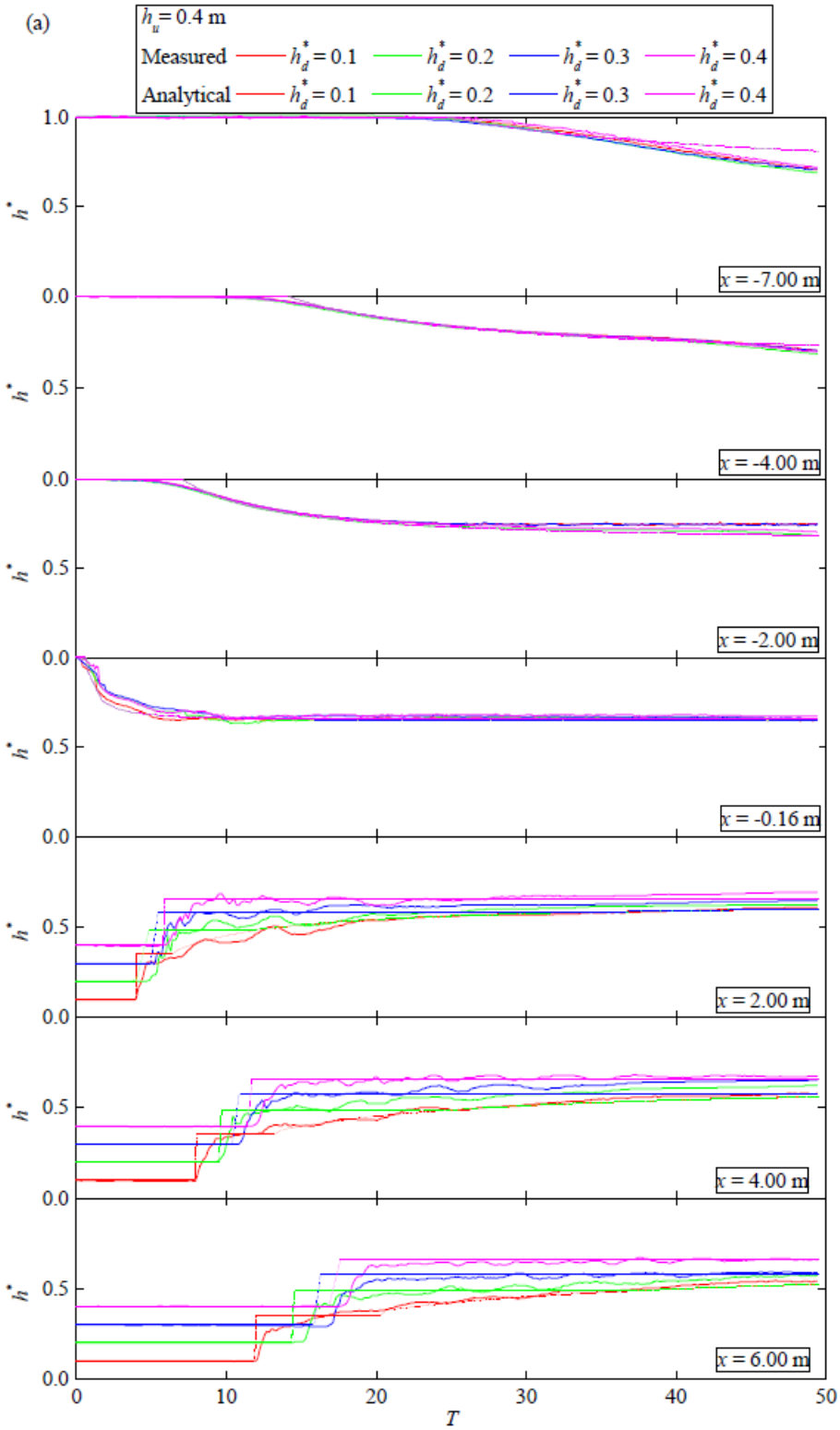
(a)
$h_u = 0.4$ m
Measured $h_d^* = 0.1$ $h_d^* = 0.2$ $h_d^* = 0.3$ $h_d^* = 0.4$
Analytical $h_d^* = 0.1$ $h_d^* = 0.2$ $h_d^* = 0.3$ $h_d^* = 0.4$
h^*
x = -7.00 m
x = -4.00 m
x = -2.00 m
x = -0.16 m
x = 2.00 m
x = 4.00 m
x = 6.00 m
T

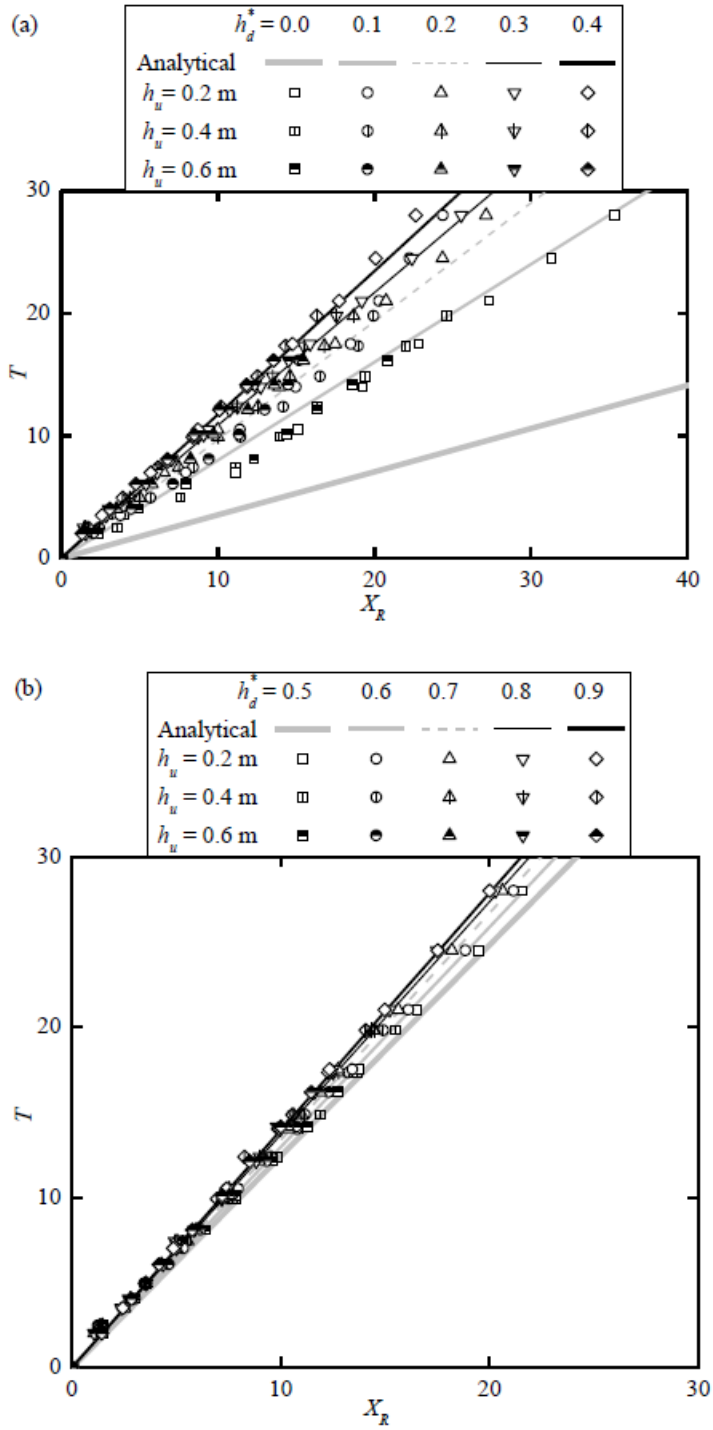

Fig. 8. Comparison of the measured and predicted locations of shock wave fronts.

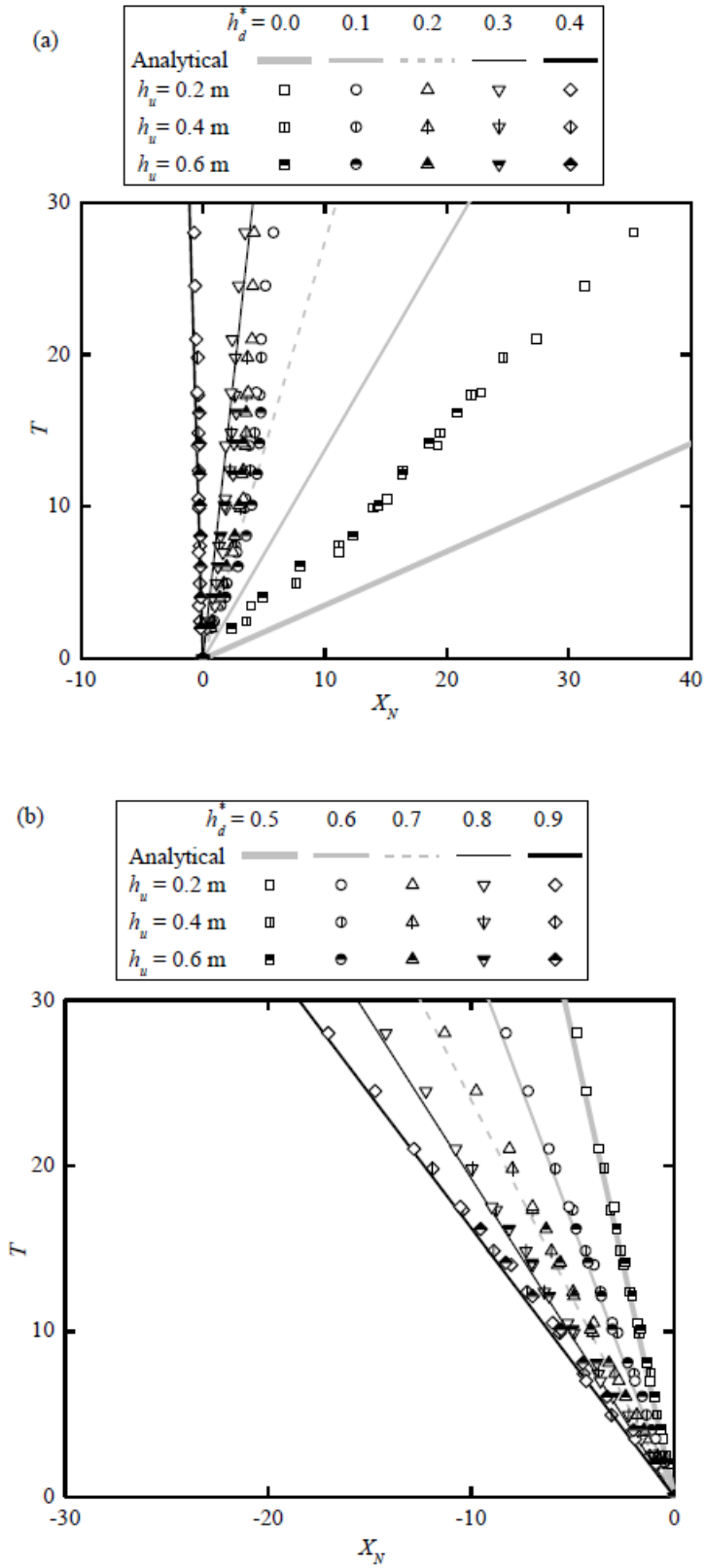

Fig. 9. Comparison of the measured and predicted locations of rarefaction wave tails.

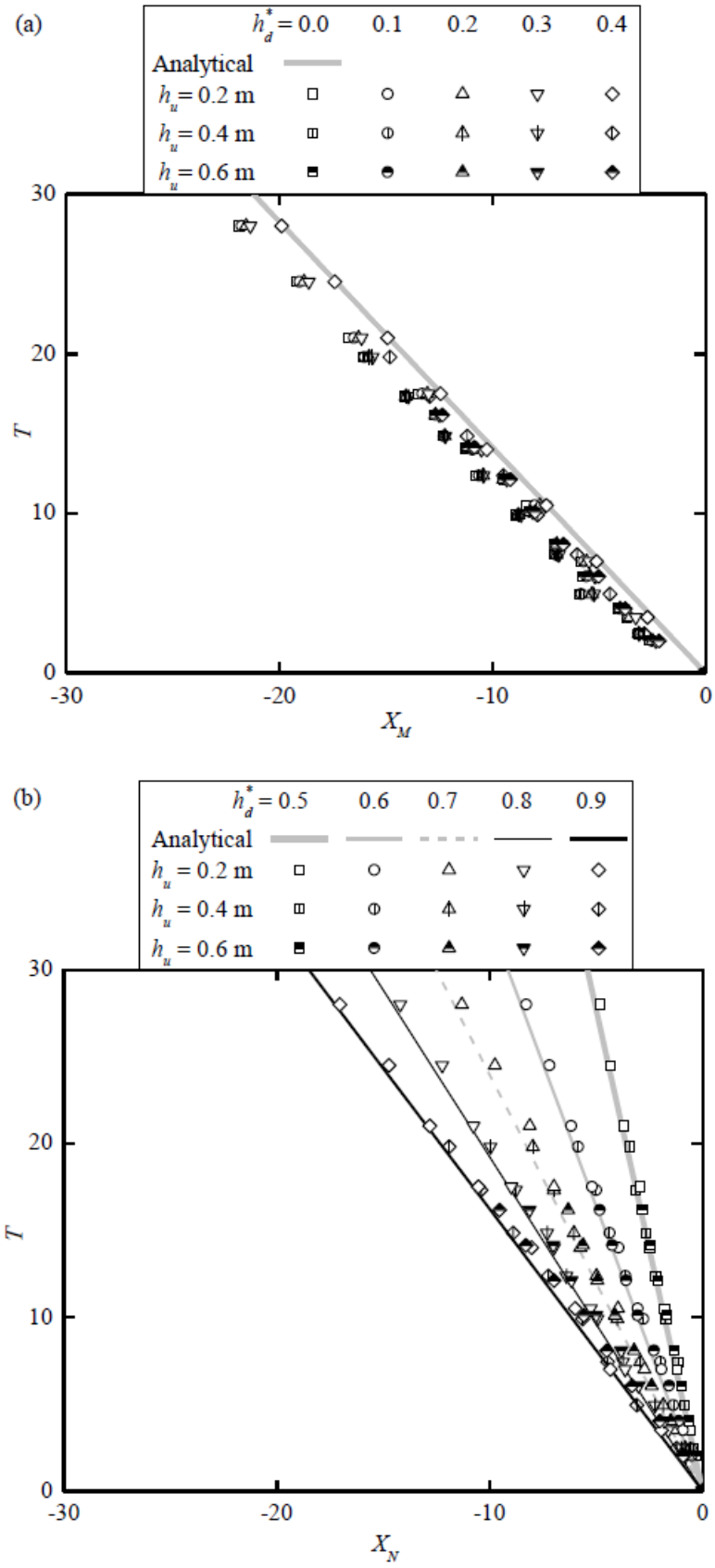

Fig. 10. Comparison of the measured and predicted locations of rarefaction wave fronts.

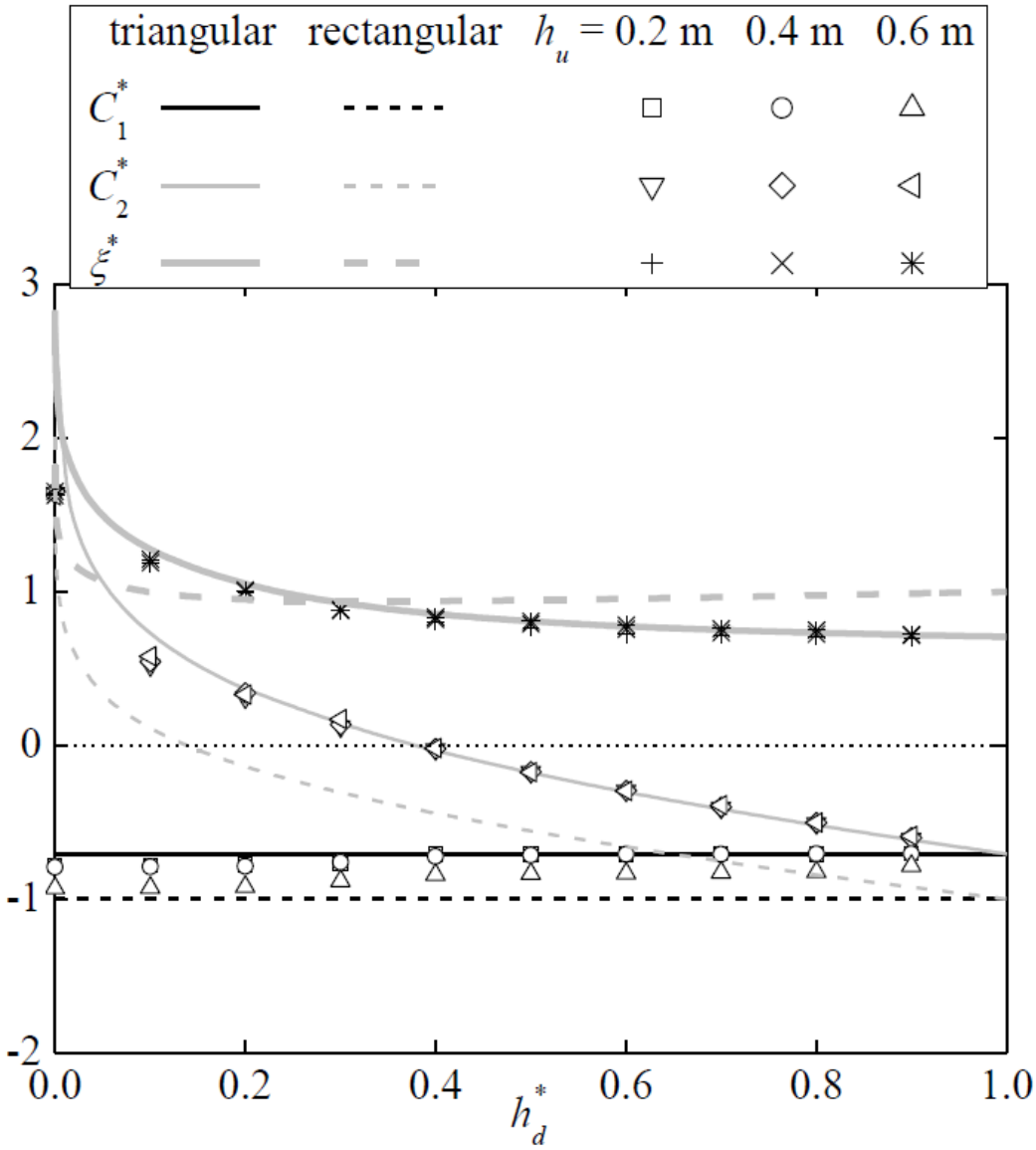

Fig. 11. Comparison of the measured and predicted C_1^*, C_2^* and ξ^*.

735